

SVarM: Linear Support Varifold Machines for Classification and Regression on Geometric Data

Emmanuel Hartman, Nicolas Charon
 Department of Mathematics
 University of Houston

June 10, 2025

Abstract

Despite progress in the rapidly developing field of geometric deep learning, performing statistical analysis on geometric data—where each observation is a shape such as a curve, graph, or surface—remains challenging due to the non-Euclidean nature of shape spaces, which are defined as equivalence classes under invariance groups. Building machine learning frameworks that incorporate such invariances, notably to shape parametrization, is often crucial to ensure generalizability of the trained models to new observations. This work proposes *SVarM* to exploit varifold representations of shapes as measures and their duality with test functions $h : \mathbb{R}^n \times S^{n-1} \rightarrow \mathbb{R}$. This method provides a general framework akin to linear support vector machines but operating instead over the infinite-dimensional space of varifolds. We develop classification and regression models on shape datasets by introducing a neural network-based representation of the trainable test function h . This approach demonstrates strong performance and robustness across various shape graph and surface datasets, achieving results comparable to state-of-the-art methods while significantly reducing the number of trainable parameters.

1 Introduction

Shape analysis, or geometric data science, is a field dedicated to building statistical and machine learning methods able to retrieve and analyze the morphological variability in geometric structures. This is a particularly central problem in applications such as computer vision or biomedical imaging where observations often come as segmented curves, surfaces, densities or other types of complex geometric data. Various approaches have been proposed, including Riemannian and elastic shape space models [21, 36, 27, 51], topology based methods [20, 13, 18], and metric/functional matching frameworks [9, 35, 37]. With the recent advances in acquisition protocols and the explosion in the size and resolution of datasets that followed, one can expect deep learning to eventually provide tools that better scale up to modern data dimensionality. Despite this, the very nature of geometric data poses unique challenges when it comes to designing robust neural network models to tackle shape analysis tasks, which is the object of active research within the relatively new area known as *geometric deep learning*, see the surveys [10, 12, 19] and references therein for the current state-of-the-art.

In this work, we introduce a shape learning framework based on a different construction than aforementioned references. The main idea is to leverage the concept of *varifolds* from geometric measure theory [2, 1] along with the natural representation of a shape $q \in \mathcal{S}$ —such as a curve or a surface in \mathbb{R}^n —as its corresponding varifold $\mu_q \in \mathcal{V}$. The mapping $q \mapsto \mu_q$ is invariant under reparameterization, thereby providing a (nonlinear) embedding of the shape space \mathcal{S} into \mathcal{V} , the

space of measures on $\mathbb{R}^n \times S^{n-1}$. This enables us to instead build the learning framework on the space of varifolds by exploiting the duality of these measures with test functions. We here simply propose to rely on linear (or affine) forms of \mathcal{V} of the form $\langle \mu, h \rangle$, where $h \in C_0(\mathbb{R}^n \times S^{n-1})$ is a trainable test function. Due to its analogy with support vector machines (but here considered in the infinite-dimensional varifold space), we coin our model **Support Varifold Machines** (SVarM) and derive formulations of the shape regression and classification problems based on this setting. Importantly, this approach allows for a principled handling of complex shapes without requiring prior regularization or registration. Additionally, by focusing on approximating continuous functions in a low-dimensional space, the model remains lightweight, requiring significantly fewer trainable parameters than traditional models operating on raw geometric data as inputs.

The presentation and contributions of the paper are organized into three main sections. Section 2 introduces the mathematical settings of shape spaces and of varifolds. We then proceed by deriving a few theoretical results related to the approximation properties of SVarM for regression and classification as well as its stability with respect to geometric perturbations. Section 3 details our proposed neural network architecture, which approximates the trainable test function h of the model. Finally, Section 4 demonstrates the practical effectiveness of the approach on various regression and classification problems for real surface and shape graph datasets.

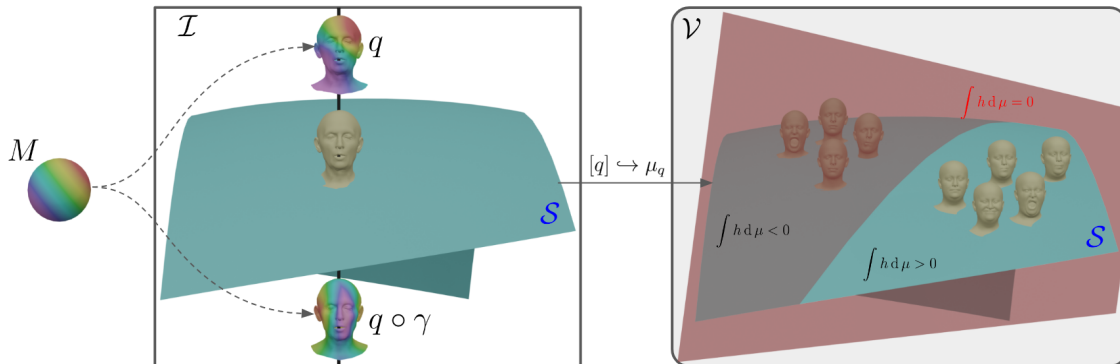


Figure 1: Representation of the quotient shape space \mathcal{S} (left) and its embedding in varifold space \mathcal{V} (right). An linear form $\mu \mapsto \langle \mu, h \rangle$ used by SVarM is visualized as the red hyperplane in \mathcal{V} .

2 Mathematical foundations and results

2.1 Shape Space

The concept of "shape" encompasses a wide variety of geometric structures (see e.g. [51, 5, 44] for general overviews on shape analysis). Although the framework we introduce can in principle apply to any type of shapes that can be viewed as measures or varifolds, our focus here will be on open/closed curves embedded in the plane or 3D space, surfaces in \mathbb{R}^3 , and by extension structures known as shape graphs [46, 3]. The challenging aspect of dealing with such objects is that there is generally not a simple nor canonical way to represent them in a common Euclidean or even functional space. Indeed, a curve or surface is usually defined by a parametrization function $q : M \rightarrow \mathbb{R}^n$, where $n = 2$ or 3 and M is the parameter manifold (for instance an interval or S^1 for open and closed curves, a disk or S^2 for open/closed surfaces...). In this paper, we will consider rectifiable shapes where q is assumed to be a bi-Lipschitz regular embedding from M to \mathbb{R}^n , denoted by $q \in \mathcal{I} \doteq \text{Emb}_{\text{Lip}}(M, \mathbb{R}^n)$. However, q itself does not uniquely identify the shape $q(M) \subseteq \mathbb{R}^n$. The

action of any reparametrization $q \circ \gamma$, where $\gamma \in \mathcal{D} = \text{Diff}_{\text{Lip}}(M)$ is a bi-Lipschitz homeomorphism of M , leaves the shape $q(M)$ invariant. In other words, the actual shape associated to q is in essence the equivalence class $[q] = \{q \circ \gamma : \gamma \in \text{Diff}_{\text{Lip}}(M)\}$, and the shape space \mathcal{S} can be thus identified with the quotient $\mathcal{S} = \mathcal{I}/\mathcal{D}$, see Figure 1 for an illustration. Note that quotienting out other shape invariances, such as to rigid motions of \mathbb{R}^n , can also be relevant in certain situations, but this work focuses on creating a parametrization-invariant model, as rigid alignment can usually be applied in a separate step. In fact, Section 4.1 and Section 4.2 illustrates how SVarM can itself be used for that very task.

We want to add that the above shape space setting also comprises discrete objects, e.g. polygonal curves and triangulated surfaces. These correspond to the case when M is subdivided into a 1- or 2-dimensional mesh and the parametrization q is a Lipschitz piecewise affine map over this mesh, in which case $q(M)$ can be seen as a reunion of adjacent cells in \mathbb{R}^n . The issue of parametrization invariance still remains very relevant in this situation. Namely, a proper learning model should exhibit some degree of robustness to operations such as mesh subdivision, simplification or resampling.

2.2 Varifolds

The concept of varifold goes back to early works in geometric measure theory, notably [2, 1], where it provided a natural and convenient setting to reframe geometric variational problems into problems on measure spaces. In more recent years, multiple works in applied mathematics have leveraged varifold representations in the context of shape registration [15, 28, 30, 45], computational geometry [26, 11, 38], or computer vision [39, 6, 23]. One of the fundamental features explaining the interest in varifolds for these different problems is that it provides a representation of shapes, both continuous and discrete, that is independent of parametrization/sampling, as we shall explain below. This suggests that it can be well-suited in the design of learning models on shape spaces.

We shall consider the following particular and simpler version of the notion of varifolds introduced in [1], similar to the framework of [28], which is specifically tailored to shapes of dimension or co-dimension 1 such as curves and surfaces that are the focus of this paper:

Definition 1. *A varifold is a positive Radon measure on $\mathbb{R}^n \times S^{n-1}$ where S^{n-1} denotes the unit sphere of \mathbb{R}^n . We shall write, in short, $\mathcal{V} \doteq \mathcal{M}^+(\mathbb{R}^n \times S^{n-1})$ the space of varifolds.*

To be exact, the above definition corresponds to dimension/codimension 1 oriented varifolds of \mathbb{R}^n ; a more general construction can be obtained by replacing S^{n-1} with Grassmannians, c.f. [1, 15]. We will then denote $\text{supp}(\mu) \subseteq \mathbb{R}^n \times S^{n-1}$ the *support* of a varifold $\mu \in \mathcal{V}$. Furthermore, by the usual Riesz-Markov-Kakutani representation theorem, any varifold μ can be viewed as an element of the dual to $C_0(\mathbb{R}^n \times S^{n-1})$, the space of continuous test functions on $\mathbb{R}^n \times S^{n-1}$ vanishing at infinity and we shall use the notation $\langle \mu, h \rangle = \int_{\mathbb{R}^n \times S^{n-1}} h(x, v) d\mu(x, v)$ for the duality bracket between \mathcal{V} and $C_0(\mathbb{R}^n \times S^{n-1})$. In particular, a Dirac varifold $\delta_{(x_0, v_0)}$ for some $(x_0, v_0) \in \mathbb{R}^n \times S^{n-1}$ is such that $\langle \delta_{(x_0, v_0)}, h \rangle = h(x_0, v_0)$.

Now, going back to shape spaces, any Lipschitz embedded curve or surface $q : M \rightarrow \mathbb{R}^n$ (where M is of dimension 1 or $n - 1$) can be canonically mapped to a varifold $\mu_q \in \mathcal{V}$ that is defined as the pushforward measure $\mu_q := (q, v_q)_* \text{vol}_q$, where v_q denotes the unit tangent/normal vector field and vol_q is the induced length/area measure on M . More explicitly, for any $h \in C_0(\mathbb{R}^n \times S^{n-1})$,

$$\langle \mu_q, h \rangle = \int_{\mathbb{R}^n \times S^{n-1}} h(x, v) d\mu_q(x, v) = \int_M h(q(m), v_q(m)) d\text{vol}_q(m).$$

Intuitively, μ_q represents the distribution of tangent/normal vectors at the different points of the shape $q(M)$ with local density given by the length/area measure along $q(M)$. A key property of the mapping $q \mapsto \mu_q$ is that only depends on the image set $q(M)$ and not reparametrizations:

Theorem 1. *For any $q \in \mathcal{I}$ and $\gamma \in \mathcal{D}$, it holds that $\mu_{q \circ \gamma} = \mu_q$. Consequently, one obtains a well-defined map $[q] \in \mathcal{S} \mapsto \mu_q \in \mathcal{V}$ which, in addition, is injective.*

Proof. This result and its proof are similar to that of previous works such as [15, 4], albeit in a slightly different setting. We recap the main arguments, most of which rely on known results from geometric measure theory. Introducing all the related definitions and concepts in detail is out of the scope of this paper and we will thus refer the reader to [43] for a precise exposition.

First, we need to show that the Var map is well-defined in the sense that μ_q is independent of the parametrization. Denoting the embedded shape $S = q(M)$, S is a rectifiable subset of \mathbb{R}^n of dimension d ($d = 1, 2$ being the dimension of the parameter space M). Then the area formula (Theorem 3.3 in [43]) implies in this case that:

$$\langle \mu_q, h \rangle = \int_M h(q(m), v_q(m)) d \text{vol}_q(m) = \int_S h(x, v_S(x)) d\mathcal{H}^d(x) \quad (1)$$

where \mathcal{H}^d denotes the d -dimensional Hausdorff measure of \mathbb{R}^n , and $v_S(x)$ is the tangent/normal vector to S at x which is defined for \mathcal{H}^d -a.a. $x \in S$. This shows that $\langle \mu_q, h \rangle$ only depends on $S = q(M)$ and not the parametrization q itself.

Next we need to prove the injectivity of the varifold map on \mathcal{S} . Let $[q], [q']$ be two distinct shapes of \mathcal{S} . Then $S = q(M)$ and $S' = q'(M)$ are two distinct rectifiable subsets of dimension d of \mathbb{R}^n . Without loss of generality, we may assume that $\mathcal{H}^d(S \setminus S') > 0$. By continuity, one can deduce that there exist $x_0 \in S$, $r > 0$ and $\epsilon > 0$ such that $\text{dist}((B(x_0, r), S')) > \epsilon > 0$. Then one can construct a nonnegative test function $h \in C_0(\mathbb{R}^n \times S^{n-1})$ such that $h(x, v) = 1$ for any $x \in B(x_0, r)$ and $h(x, v) = 0$ for $\|x - x_0\| \geq r + \epsilon$. From (1), we obtain that:

$$\langle \mu_q, h \rangle = \int_S h(x, v_S(x)) d\mathcal{H}^d(x) \geq \int_{B(x_0, r) \cap S} h(x, v_S(x)) d\mathcal{H}^d(x) = \mathcal{H}^d(B(x_0, r) \cap S) > 0$$

while

$$\langle \mu_{q'}, h \rangle = \int_{S'} h(x, v_{S'}(x)) d\mathcal{H}^d(x) = 0$$

since the support of h does not intersect S' by construction. It follows that $\langle \mu_q, h \rangle \neq \langle \mu_{q'}, h \rangle$ and thus the two varifolds μ_q and $\mu_{q'}$ are distinct in \mathcal{V} . \square

This property will be fundamental for what follows, as it allows us to embed any shape of \mathcal{S} into \mathcal{V} (see Figure 1) and exploit the dual nature of \mathcal{V} .

Another advantage of the varifold framework is that it applies very naturally to the discrete geometric setting as well. Specifically, when q is a piecewise affine embedding defined over a polyhedral mesh on M , the shape $q(M)$ is made of a reunion of polyhedral cells $\{F_i\}$ in \mathbb{R}^n (segments or triangles) which can each be approximated by a single weighted Dirac varifold $w_i \delta_{(x_i, v_i)}$, with $x_i \in \mathbb{R}^n$, $v_i \in S^{n-1}$ and $w_i > 0$ being respectively the center of mass, unit tangent/normal vector and length/area of F_i . This leads to a discrete varifold approximation $\mu_q \approx \sum_i w_i \delta_{(x_i, v_i)}$ of q . This type of approximations in \mathcal{V} has been routinely used and analyzed in works such as [28, 11, 38], to which we refer for more details.

2.3 Theoretical Properties of SVarM

2.3.1 Existence of Regression Functions and Separators

Some important theoretical questions when it comes to the proposed approach are to understand the class of regression and classification functions that are modeled by SVarM and what sets of varifolds or shapes can be separated in this framework. In this section, we present a few results in this direction.

Let us first recall a few definitions related to the different topologies on varifolds. The space of signed measures $\mathcal{M}(\mathbb{R}^n \times S^{n-1})$ can be identified with the topological dual to the space of test functions $C_0(\mathbb{R}^n \times S^{n-1})$ equipped with the $\|\cdot\|_\infty$ norm. As such, different topologies are usually considered on $\mathcal{M}(\mathbb{R}^n \times S^{n-1})$ and by restriction on \mathcal{V} . The first of which is the dual metric topology, i.e. the topology induced by the *total variation* norm:

$$\|\mu\|_{TV} = \sup_{\|h\|_\infty \leq 1} |\langle \mu, h \rangle| = |\mu|(\mathbb{R}^n \times S^{n-1})$$

In particular, for a varifold μ_q associated to $q \in \mathcal{I}$, one can see from (1) that $\|\mu_q\|_{TV}$ is the total length/area of the shape $q(M)$. The TV norm induces a rather strong topology on varifolds: for instance, the TV norm between two Dirac masses $\delta_{(x_0, v_0)}$ and $\delta_{(x_1, v_1)}$ is 2 whenever $(x_0, v_0) \neq (x_1, v_1)$ and 0 when the position and direction coincide. It is often more natural to consider the *weak-** topology on $\mathcal{M}(\mathbb{R}^n \times S^{n-1})$. By definition, a sequence (μ_i) weak- $*$ converges to μ , denoted $\mu_i \xrightarrow{*} \mu$, when $\langle \mu_i, h \rangle \xrightarrow{i \rightarrow \infty} \langle \mu, h \rangle$ for all $h \in C_0(\mathbb{R}^n \times S^{n-1})$. Note that the weak- $*$ convergence can be also locally metrized by a variety of usual metrics on $\mathcal{M}(\mathbb{R}^n \times S^{n-1})$ such as the bounded Lipschitz norm or the Wasserstein metrics of optimal transport (for normalized measures), c.f. [48] Chap. 6.

As a consequence of standard results on Banach spaces and weak- $*$ topology, specifically Proposition 3.14 in [8], any linear function $\mathcal{V} \rightarrow \mathbb{R}$ that is continuous with respect to the weak- $*$ convergence is necessarily of the form $\mu \mapsto \langle \mu, h \rangle$ for some test function $h \in C_0(\mathbb{R}^n \times S^{n-1})$. It follows that the set of affine weak- $*$ continuous functions $\varphi : \mathcal{V} \rightarrow \mathbb{R}$ are of the form $\varphi(\mu) = \langle \mu, h \rangle + \beta$ for some $h \in C_0(\mathbb{R}^n \times S^{n-1})$ and $\beta \in \mathbb{R}$. Thus we have the following:

Proposition 1. *The set of functionals modeled by SVarM are exactly the affine weak- $*$ continuous functionals on \mathcal{V} .*

However, this does not hold anymore when the continuity is with respect to the stronger TV metric topology due to the lack of reflexivity of \mathcal{V} . In that case, one can only recover the following approximation bound over any finite set of varifolds:

Proposition 2. *Suppose $\varphi : \mathcal{V} \rightarrow \mathbb{R}$ is an affine function and continuous with respect to the TV norm topology and fix $C \subseteq \mathcal{V}$ any finite subset of the space of varifolds. For all $\epsilon > 0$, there exists $h \in C_0(\mathbb{R}^n \times S^{n-1}, \mathbb{R})$ and $\beta \in \mathbb{R}$ such that*

$$\sup_{\mu \in C} |\varphi(\mu) - (\langle \mu, h \rangle + \beta)| < \epsilon.$$

Proof. Let us first consider the case of linear forms i.e. let $\varphi : \mathcal{M}(\mathbb{R}^n \times S^{n-1}) \rightarrow \mathbb{R}$ be a continuous linear functional, in other words φ belongs to the bidual space $C_0(\mathbb{R}^n \times S^{n-1}, \mathbb{R})^{**}$. By Goldstine theorem [42], $C_0(\mathbb{R}^n \times S^{n-1}, \mathbb{R})$ is dense in its bi-dual with respect to the weak- $*$ topology on $C_0(\mathbb{R}^n \times S^{n-1}, \mathbb{R})^{**}$. Specifically, for the canonical embedding J defined by:

$$\begin{aligned} J : C_0(\mathbb{R}^n \times S^{n-1}, \mathbb{R}) &\rightarrow C_0(\mathbb{R}^n \times S^{n-1}, \mathbb{R})^{**} \\ h &\mapsto (\mu \in \mathcal{M}(\mathbb{R}^n \times S^{n-1}) \mapsto \langle \mu, h \rangle) \end{aligned}$$

we have $J(C_0(\mathbb{R}^n \times S^{n-1}, \mathbb{R}))$ dense in $C_0(\mathbb{R}^n \times S^{n-1}, \mathbb{R})^{**}$. Consequently, we can find a sequence $(h_i) \subseteq C_0(\mathbb{R}^n \times S^{n-1}, \mathbb{R})$ so that $J(h_i)(\mu) = \langle \mu, h_i \rangle \rightarrow \varphi(\mu)$ as $i \rightarrow \infty$ for all $\mu \in \mathcal{M}(\mathbb{R}^n \times S^{n-1})$. Now, since C is assumed to be finite, choosing i large enough so that $|\varphi(\mu) - \langle \mu, h_i \rangle| < \epsilon$ for all $\mu \in C$ leads to the desired results. The extension to affine continuous functionals is then straightforward by incorporating the extra bias term $\beta \in \mathbb{R}$. \square

For classification problems, we are interested in determining when two given sets of varifolds (or shapes) can be separated by SVarM.

Definition 2. *Two disjoint sets $C_1, C_2 \subseteq \mathcal{V}$ are strictly separated by some test function h when:*

$$\sup_{\mu \in C_1} \langle \mu, h \rangle < \inf_{\nu \in C_2} \langle \nu, h \rangle \quad (2)$$

Note that by introducing the extra bias parameter $\beta \in \mathbb{R}$, the above could be reformulated equivalently as $\sup_{\mu \in C_1} \langle \mu, h \rangle + \beta < 0 < \inf_{\nu \in C_2} \langle \nu, h \rangle + \beta$, i.e. in a way analogous to separation by a hyperplane in classical SVM. A first generic result, that follows from the Hahn-Banach separation theorem is:

Theorem 2. *Suppose $C_1, C_2 \subseteq \mathcal{V}$ are convex weak-* compact subsets such that $C_1 \cap C_2 = \emptyset$. Then there exists a test function $h \in C_0(\mathbb{R}^n \times S^{n-1}, \mathbb{R})$ that separates C_1 and C_2 in the sense of (2).*

Proof. Let $C_1, C_2 \subseteq \mathcal{M}(\mathbb{R}^n \times S^{n-1})$ be convex weak-* compact subsets such that $C_1 \cap C_2 = \emptyset$. Since the space $\mathcal{M}(\mathbb{R}^n \times S^{n-1})$ with the weak-* topology is a locally convex space, the Hahn-Banach separation theorem (Theorem 1.7 in [8]) applies and there exists a weak-* continuous linear form $\varphi : \mathcal{V} \rightarrow \mathbb{R}$ such that:

$$\sup_{\mu \in C_1} \varphi(\mu) < \inf_{\nu \in C_2} \varphi(\nu).$$

As already noted above, φ must be of the form $\varphi(\mu) = \langle \mu, h \rangle$ for some test function $h \in C_0(\mathbb{R}^n \times S^{n-1}, \mathbb{R})$, which leads to the result. \square

The weak-* compactness assumption is relatively natural as, by the Banach-Alaoglu theorem, closed sets of varifolds with bounded total variation are in particular weak-* compact. However, the condition of convexity in \mathcal{V} in Theorem 2 is rather abstract and not immediate to connect to concrete situations of interest. We will thus look to derive more specific conditions for certain families of measure sets C_1 and C_2 . First of all, we can focus on the situation where C_1 and C_2 are both finite subsets of \mathcal{V} , which is natural when considering classification and regression problems in practice. In that case, C_1 and C_2 are automatically weak-* compact. We can then state the following simpler condition:

Theorem 3. *Let $C_1, C_2 \subseteq \mathcal{V}$ be disjoint finite sets of varifolds which satisfy the property that either 1) for each $\nu \in C_2$, $\text{supp}(\nu) \not\subseteq \bigcup_{\mu \in C_1} \text{supp}(\mu)$ or 2) for each $\mu \in C_1$, $\text{supp}(\mu) \not\subseteq \bigcup_{\nu \in C_2} \text{supp}(\nu)$. Then there exists $h \in C_0(\mathbb{R}^n \times S^{n-1}, \mathbb{R})$ that separates C_1 and C_2 .*

Proof. Without loss of generality, let us assume that $C_1, C_2 \subseteq \mathcal{S}$ are two finite sets in \mathcal{V} with $C_1 = \{\mu_1, \dots, \mu_p\}$ and $C_2 = \{\nu_1, \dots, \nu_q\}$, such that for each $\nu \in C_2$, $\text{supp}(\nu) \not\subseteq \bigcup_{\mu \in C_1} \text{supp}(\mu)$. Let us denote by $\text{conv}(C_1)$ and $\text{conv}(C_2)$ the convex hulls of the two sets C_1 and C_2 in \mathcal{V} . By contradiction, if $\text{conv}(C_1) \cap \text{conv}(C_2) \neq \emptyset$, there exist $(\alpha_1, \dots, \alpha_p)$ and $(\beta_1, \dots, \beta_q)$ in the probability simplexes of \mathbb{R}_+^p and \mathbb{R}_+^q respectively such that:

$$\sum_{i=1}^p \alpha_i \mu_i = \sum_{j=1}^q \beta_j \nu_j \implies \text{supp} \left(\sum_{j=1}^q \beta_j \nu_j \right) = \text{supp} \left(\sum_{i=1}^p \alpha_i \mu_i \right)$$

Now, on the one hand, $\text{supp}(\sum_{i=1}^p \alpha_i \mu_i) \subseteq \bigcup_{\mu \in C_1} \text{supp}(\mu)$. On the other hand, we have:

$$\text{supp}\left(\sum_{j=1}^q \beta_j \nu_j\right) = \bigcup_{j: \beta_j \neq 0} \text{supp}(\nu_j).$$

Since not all β_j 's can be 0, we deduce that there exist j such that $\text{supp}(\nu_j) \subseteq \bigcup_{\mu \in C_1} \text{supp}(\mu)$ which contradicts the assumption. Therefore, $\text{conv}(C_1)$ and $\text{conv}(C_2)$ are two disjoint convex sets in \mathcal{V} . They are also weak-* compact as the convex hulls of finite sets; indeed $\text{conv}(C_1)$ is the image of the compact probability simplex by the continuous map $(\alpha_1, \dots, \alpha_p) \mapsto \sum_{i=1}^p \alpha_i \mu_i$, and similarly for $\text{conv}(C_2)$. Then, by Theorem 2, we deduce that $\text{conv}(C_1)$ and $\text{conv}(C_2)$ and thus C_1 and C_2 can be separated by a test function $h \in C_0(\mathbb{R}^n \times S^{n-1})$. \square

Remark 1. *Note that this only provides a sufficient but not necessary condition of separability. For instance, if C_1 and C_2 are both made of varifolds all having the same compact support set $K \subseteq \mathbb{R}^n \times S^{n-1}$ but such that their total mass satisfy $\mu(K) < \nu(K)$ for all $\mu \in C_1$ and $\nu \in C_2$, then C_1 and C_2 are still separable by taking any test function h that is constant equal to 1 on K .*

The above condition on the support of the varifolds becomes even more explicit when considering varifolds that are associated to continuous shapes via the mapping $q \in \mathcal{I} \mapsto \mu_q$ introduced in Section 2.2. We get specifically:

Corollary 1. *Let Σ_1, Σ_2 be finite sets of continuous shapes in \mathcal{S} such that either 1) for each $q' \in \Sigma_2$, $q'(M) \not\subseteq \bigcup_{q \in \Sigma_1} q(M)$ or 2) for each $q \in \Sigma_1$, $q(M) \not\subseteq \bigcup_{q' \in \Sigma_2} q'(M)$. Then the two sets Σ_1, Σ_2 are strictly separable by a test function $h \in C_0(\mathbb{R}^n \times S^{n-1}, \mathbb{R})$.*

This indeed follows directly from Theorem 3 since for $q \in \mathcal{I}$, $\text{supp}(\mu_q) = \{(q(m), v_q(m)) : m \in M\}$ and thus the assumption of Corollary 1 implies the assumption of Theorem 3.

Remark 2. *When the condition of Corollary 1 is not verified, it is possible to find sets that are not separable within the SVarM setting. Figure 2 shows such an example in which the two sets (green and red), each made of two shapes, cannot be separated. This is because the two convex hulls of the varifolds associated to the shapes in those sets do intersect in \mathcal{V} ; specifically, one can see that the varifold $\frac{1}{2}\mu_{q_1} + \frac{1}{2}\mu_{q_2}$, q_1 and q_2 being the two shapes of the first (green) set, is equal to $\frac{1}{2}\mu_{q'_1} + \frac{1}{2}\mu_{q'_2}$ where q'_1 and q'_2 are the two shapes in the second (red) set, and therefore belongs to the intersection of the two convex hulls. This example further shows that the weaker and somewhat more natural condition that the support of any varifold in one of the two sets is not included in the support of any varifold from the other set is not sufficient to guarantee separability by SVarM since the example of Figure 2 is not separable and does satisfy this condition (but does not satisfy that of Corollary 1).*

One can also obtain a corresponding result for discrete varifolds such as varifolds approximating discrete meshes. It is formulated below and is again a direct corollary of Theorem 3:

Corollary 2. *Let C_1 and C_2 be two finite sets of discrete varifolds that are given by $C_1 = \left\{ \sum_{i=1}^{N_k} r_i^{(k)} \delta_{(x_i^{(k)}, v_i^{(k)})} \right\}_{k=1, \dots, K_1}$ and $C_2 = \left\{ \sum_{i=1}^{\tilde{N}_k} \tilde{r}_i^{(k)} \delta_{(\tilde{x}_i^{(k)}, \tilde{v}_i^{(k)})} \right\}_{k=1, \dots, K_2}$. Assume that these sets satisfy either of the two following conditions:*

1. *For each $k = 1, \dots, K_1$, $\{(x_i^{(k)}, v_i^{(k)}), i = 1, \dots, N_k\} \not\subseteq \bigcup_{l=1}^{K_2} \{(\tilde{x}_i^{(l)}, \tilde{v}_i^{(l)}), i = 1, \dots, \tilde{N}_l\}$*
2. *For each $k = 1, \dots, K_2$, $\{(\tilde{x}_i^{(k)}, \tilde{v}_i^{(k)}), i = 1, \dots, \tilde{N}_k\} \not\subseteq \bigcup_{l=1}^{K_1} \{(x_i^{(l)}, v_i^{(l)}), i = 1, \dots, N_l\}$*

Then the two sets C_1, C_2 are separable by a test function $h \in C_0(\mathbb{R}^n \times S^{n-1}, \mathbb{R})$.

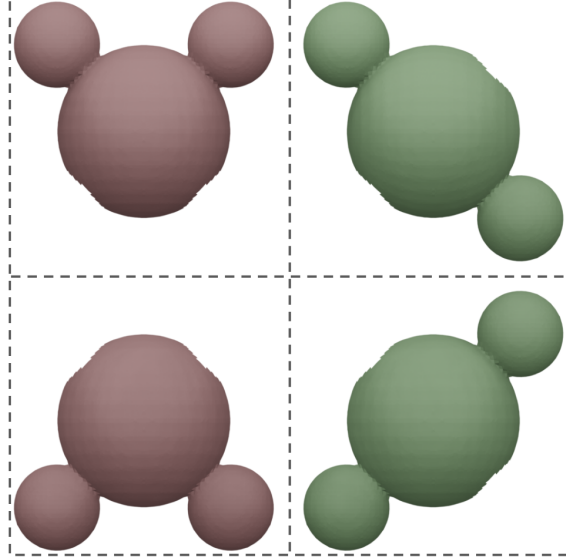


Figure 2: An example of two sets of shapes (in green and red) that cannot be separated within the SVarM framework. Note also that neither shape in one set is a subset of a shape from the other set, showing that this is not a sufficient condition of separability for SVarM.

2.3.2 Stability with Respect to Shape Deformations and Perturbations

Another key theoretical question regarding the SVarM approach is the stability of the model under perturbations of the input data. We show below that this type of result can hold under the assumption that h is Lipschitz continuous. As described in Section 3, we will approximate h using a multilayer perceptron (MLP) architecture. For fixed weights (i.e., after training), an MLP is a Lipschitz function, and one can efficiently compute an upper bound on its Lipschitz constant [49]. Let us first examine stability for general varifolds in \mathcal{V} :

Theorem 4. *Let $\mu, \nu \in \mathcal{V}$ and $h \in C_0(\mathbb{R}^n \times S^{n-1})$ such that h is Lipschitz with constant K . Then,*

$$|\langle \mu, h \rangle - \langle \nu, h \rangle| \leq \|h\|_\infty \cdot \|\mu - \nu\|_{TV}$$

and

$$|\langle \mu, h \rangle - \langle \nu, h \rangle| \leq \left| \|\mu\|_{TV} - \|\nu\|_{TV} \right| \cdot \|h\|_\infty + \|\mu\|_{TV} \cdot K \cdot W_1 \left(\frac{\mu}{m_\mu}, \frac{\nu}{m_\nu} \right)$$

where W_1 denotes the 1-Wasserstein distance.

Proof. Let $\mu, \nu \in \mathcal{V}$ and $h \in C_0(\mathbb{R}^n \times S^{n-1})$ such that h is Lipschitz with constant K .

Bound 1: Based on the definition of the TV norm on $\mathcal{M}(\mathbb{R}^n \times S^{n-1})$ given above, we can bound the difference in the evaluation of μ and ν on $h \neq 0$ as follows:

$$\begin{aligned} |\langle \mu, h \rangle - \langle \nu, h \rangle| &= \left| \int_{\mathbb{R}^n \times S^{n-1}} h \, d\mu - \int_{\mathbb{R}^n \times S^{n-1}} h \, d\nu \right| \\ &= \left| \int_{\mathbb{R}^n \times S^{n-1}} h \, d(\mu - \nu) \right| \\ &= \left| \int_{\mathbb{R}^n \times S^{n-1}} \frac{h}{\|h\|_\infty} \, d(\mu - \nu) \right| \|h\|_\infty \\ &\leq \|\mu - \nu\|_{TV} \|h\|_\infty. \end{aligned}$$

Bound 2: For brevity, let us define the total masses $m_\mu = \|\mu\|_{\text{TV}}, m_\nu = \|\nu\|_{\text{TV}}$ and the corresponding normalized measures $\bar{\mu} = \frac{\mu}{m_\mu}, \bar{\nu} = \frac{\nu}{m_\nu}$. We begin by with a series of inequalities:

$$\begin{aligned}
|\langle \mu, h \rangle - \langle \nu, h \rangle| &= |m_\mu \langle \bar{\mu}, h \rangle - m_\nu \langle \bar{\nu}, h \rangle| \\
&= |m_\mu \langle \bar{\mu}, h \rangle - m_\mu \langle \bar{\nu}, h \rangle + m_\mu \langle \bar{\nu}, h \rangle - m_\nu \langle \bar{\nu}, h \rangle| \\
&\leq |m_\mu \langle \bar{\nu}, h \rangle - m_\nu \langle \bar{\nu}, h \rangle| + |m_\mu \langle \bar{\mu}, h \rangle - m_\mu \langle \bar{\nu}, h \rangle| \\
&\leq |m_\mu - m_\nu| \cdot \left| \int_{\mathbb{R}^n \times S^{n-1}} h \, d\bar{\nu} \right| + m_\mu \left| \int_{\mathbb{R}^n \times S^{n-1}} h \, d\bar{\mu} - \int_{\mathbb{R}^n \times S^{n-1}} h \, d\bar{\nu} \right| \\
&\leq |m_\mu - m_\nu| \cdot \|h\|_\infty + m_\mu \left| \int_{\mathbb{R}^n \times S^{n-1}} h \, d\bar{\mu} - \int_{\mathbb{R}^n \times S^{n-1}} h \, d\bar{\nu} \right|.
\end{aligned}$$

Next we define the function $\bar{h} := \frac{h}{K}$. Since the Lipschitz constant of h is K , it follows that \bar{h} is 1-Lipchitz. Thus we can write

$$\left| \int_{\mathbb{R}^n \times S^{n-1}} h \, d\bar{\mu} - \int_{\mathbb{R}^n \times S^{n-1}} h \, d\bar{\nu} \right| = K \left| \int_{\mathbb{R}^n \times S^{n-1}} \bar{h} \, d\bar{\mu} - \int_{\mathbb{R}^n \times S^{n-1}} \bar{h} \, d\bar{\nu} \right|.$$

By the Kantorovich-Rubinstein formulation of the 1-Wasserstein distance,

$$W_1(\bar{\mu}, \bar{\nu}) = \sup_{\|f\|_{W^{1,\infty}} \leq 1} \left| \int_{\mathbb{R}^n \times S^{n-1}} f \, d\bar{\mu} - \int_{\mathbb{R}^n \times S^{n-1}} f \, d\bar{\nu} \right| \geq \left| \int_{\mathbb{R}^n \times S^{n-1}} \bar{h} \, d\bar{\mu} - \int_{\mathbb{R}^n \times S^{n-1}} \bar{h} \, d\bar{\nu} \right|$$

and we conclude that:

$$|\langle \mu, h \rangle - \langle \nu, h \rangle| \leq |m_\mu - m_\nu| \cdot \|h\|_\infty + m_\mu \cdot K \cdot W_1(\bar{\mu}, \bar{\nu}).$$

□

The first bound involving the total variation between μ and ν implies stability of $\langle \mu, h \rangle$ under partial occlusion of some parts of a shape (c.f. experiments of Section 4.5) while the second bound can be thought of as a control of the changes in $\langle \mu, h \rangle$ under variations of the total mass and support. Our second result demonstrates that the outputs of SVarM are stable in the space of shapes with respect to sufficiently regular perturbations in \mathcal{S} :

Theorem 5. *Let $h \in C_0(\mathbb{R}^n \times S^{n-1})$ such that h is Lipschitz with constant K and q, q' be bi-Lipschitz embeddings from a d -dimensional manifold M into \mathbb{R}^n (with either $d = 1$ or $d = n - 1$) such that $\|q - q'\|_{W^{1,\infty}} \leq C$. Then*

$$|\langle \mu_q, h \rangle - \langle \mu_{q'}, h \rangle| \leq CA_q(K\sqrt{2dL^{2d-1} + 1} + d^{d+1/2}L^{2d+1}\|h\|_\infty)$$

where $A_q = \int_M \text{dvol}_q$ is the total length/area of $q(M)$, and L the maximum of the Lipschitz constants of q and q' .

Proof. Let $h \in C_0(\mathbb{R}^n \times S^{n-1})$ such that h is Lipschitz with constant K and q, q' be bi-Lipschitz embeddings from a d -dimensional manifold M into \mathbb{R}^n such that $\|q - q'\|_{W^{1,\infty}} \leq C$. We estimate the difference between the actions of the varifolds associated with q and q' on h by:

$$\begin{aligned}
|\langle \mu_q, h \rangle - \langle \mu_{q'}, h \rangle| &= \left| \int_M h(q, n_q) \, \text{dvol}_q - \int_M h(q', n_{q'}) \, \text{dvol}_{q'} \right| \\
&= \left| \int_M h(q, n_q) \sqrt{|Jq|} - h(q', n_{q'}) \sqrt{|Jq|} + h(q', n_{q'}) \sqrt{|Jq|} - h(q', n_{q'}) \sqrt{|Jq'|} \, \text{d}m \right| \\
&\leq \int_M |h(q, n_q) - h(q', n_{q'})| \sqrt{|Jq|} \, \text{d}m + \int_M |h(q, n_q)| \frac{|\sqrt{|Jq|} - \sqrt{|Jq'|}|}{\sqrt{|Jq|}} \sqrt{|Jq|} \, \text{d}m.
\end{aligned}$$

where $Jq(m) = Dq(m)^T Dq(m)$ and $|Jq(m)|$ is the absolute value of the determinant of $Jq(m)$. Since q, q' are bi-Lipchitz embeddings, there exists $L > 0$ such that the singular values of Dq and Dq' are in $[1/L, L]$ almost everywhere on M . Therefore, for almost every $m \in M$, $\frac{1}{L^d} < \sqrt{|Jq|}, \sqrt{|Jq'|} < L^d$ and $\frac{\sqrt{d}}{L} < \|Dq\|, \|Dq'\| < \sqrt{d}L$. Moreover, for almost every $m \in M$,

$$\frac{|\sqrt{|Jq|} - \sqrt{|Jq'|}|}{\sqrt{|Jq|}} \leq \frac{L^{2d}}{2} \|Jq - Jq'\|.$$

As follows from the Hadamard inequality on determinants, one has the following bounds on the difference of the Jacobians:

$$\begin{aligned} \|Jq - Jq'\| &\leq \|Jq - Jq'\| \frac{\|Jq\|^d - \|Jq'\|^d}{\|Jq\| - \|Jq'\|} \\ &\leq d\|Jq - Jq'\| \max(\|Jq\|^{d-1}, \|Jq'\|^{d-1}) \leq d\|Jq - Jq'\|(\sqrt{d}L)^{2(d-1)} \\ &= d^d\|Jq - Jq'\|L^{2(d-1)}. \end{aligned}$$

Moreover,

$$\|Jq - Jq'\| \leq (\|Dq\| + \|Dq'\|)\|Dq - Dq'\| \leq 2\sqrt{d}LC.$$

So,

$$\int_M |h(q, n_q)| \frac{|\sqrt{|Jq|} - \sqrt{|Jq'|}|}{\sqrt{|Jq|}} \sqrt{|Jq|} \, dm \leq d^{d+1/2}CL^{2d+1} \int_M |h(q, n_q)| \sqrt{|Jq|} \, dm \leq d^{d+1/2}CL^{2d+1}\|h\|_\infty A_q.$$

where $A_q = \int_M \sqrt{|Jq|} \, dm = \int_M \text{dvol}_q$. Moreover, n_q is the unit normal vector of q computed by $n_q = \frac{\partial_1 q \wedge \dots \wedge \partial_d q}{\sqrt{|Jq|}}$. Therefore, for almost every $m \in M$,

$$\begin{aligned} \|n_q - n_{q'}\| &\leq 2L^d \|(\partial_1 q \wedge \dots \wedge \partial_d q) - (\partial_1 q' \wedge \dots \wedge \partial_d q')\| \leq 2L^d \sum_{i=1}^d \|(\partial_1 q \wedge \dots \wedge (\partial_i q - \partial_i q') \wedge \dots \wedge \partial_d q')\| \\ &\leq 2L^d \sum_{i=1}^d \|\partial_1 q\| \cdot \dots \cdot \|\partial_i q - \partial_i q'\| \cdot \dots \cdot \|\partial_d q'\| \leq 2dL^{2d-1}\|Dq - Dq'\| \leq 2dL^d C. \end{aligned}$$

where we have again used Hadamard's inequality to bound the norm of the exterior product. So, $\sqrt{\|q - q'\|^2 + \|n_q - n_{q'}\|^2} \leq C\sqrt{2dL^{2d-1} + 1}$ almost everywhere. Since h is Lipschitz with constant K , we have for almost every $m \in M$,

$$|h(q, n_q) - h(q', n_{q'})| \leq K\sqrt{\|q - q'\|^2 + \|n_q - n_{q'}\|^2} \leq CK\sqrt{2dL^{2d-1} + 1}.$$

Therefore,

$$\int_M |h(q, n_q) - h(q', n_{q'})| \sqrt{|Jq|} \, dm \leq CK\sqrt{2dL^{2d-1} + 1} \int_M \sqrt{|Jq|} \, dm = CK A_q \sqrt{2dL^{2d-1} + 1}$$

Thus, we have obtained that:

$$|\langle \mu_q, h \rangle - \langle \mu_{q'}, h \rangle| \leq C A_q (K\sqrt{2dL^{2d-1} + 1} + d^{d+1/2}L^{2d+1}\|h\|_\infty).$$

□

3 Model Architecture

The core of our regression model architecture is to approximate a map $h : \mathbb{R}^n \times S^{n-1} \rightarrow \mathbb{R}$ (for $n = 2$ or 3) which can itself approximate any affine map on \mathcal{V} as shown in Theorem ???. We perform this approximation using a multilevel perceptron (MLP) $h_\theta : \mathbb{R}^{2n} \rightarrow \mathbb{R}$ where θ denotes the trainable parameters of the MLP. It is then straightforward, based on the many existing universal approximation and expressivity theorems [25, 17, 24, 32], to rephrase all the results of Section 2.3 for functions h that are expressible by a sufficiently wide and/or deep MLP.

Given a discrete varifold $\mu = \sum_{i=1}^m w_i \delta_{(x_i, v_i)}$, we pass each support $(x_i, v_i) \in \mathbb{R}^n \times S^{n-1} \subseteq \mathbb{R}^{2n}$ through our MLP to compute a vector $H = [h_\theta(x_1, v_1), \dots, h_\theta(x_m, v_m)]$. We then view the weights of μ as a vector $W = [w_1, \dots, w_m]$ and compute

$$H^T W + \beta = \sum_{i=1}^m w_i h_\theta(x_i, v_i) + \beta = \langle \mu, h_\theta \rangle + \beta$$

where β is a trainable bias term. For the linear regression problem in \mathcal{V} , we then train this model in a supervised manner by which, given a set of varifolds $\{\mu_1, \dots, \mu_R\}$ (computed from the corresponding input shapes) and the associated labels $\{y_1, \dots, y_R\}$, we minimize the mean squared error loss

$$\text{MSE}(\theta, \beta) = \frac{1}{R} \sum_{j=1}^R (\langle \mu_j, h_\theta \rangle + \beta - y_j)^2.$$

To perform multi-class classification of varifolds, we slightly modify the architecture to learn

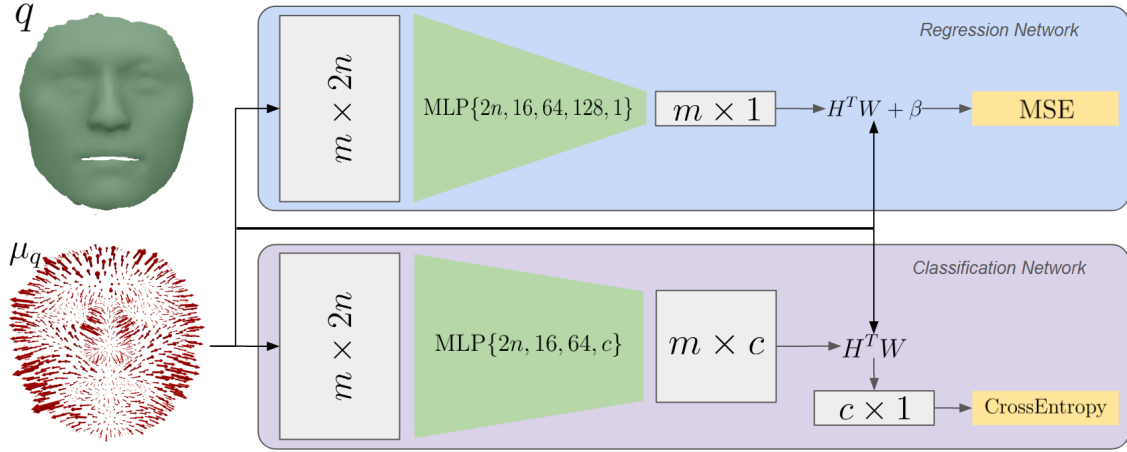


Figure 3: Model Summary: A mesh q is mapped to its varifold representation μ_q . The supports of the varifold are passed through an MLP and the resulting values are integrated with respect to the masses of μ_q . For regression, a trainable bias term is added to integral. For classification, the integral produces a c -dimensional vector viewed as logits of the probability that q belongs to each class.

a vector valued functions $h : \mathbb{R}^n \times S^{n-1} \rightarrow \mathbb{R}^c$ where $\int_{\mathbb{R}^n \times S^{n-1}} h d\mu$ is a c -dimensional vector where each entry is interpreted as a logit of the probability that μ belongs to the corresponding class. The function h is again modeled via a multi-layer perceptron (MLP) $h_\theta : \mathbb{R}^{2n} \rightarrow \mathbb{R}^c$. For $\mu = \sum_{i=1}^m w_i \delta_{(x_i, u_i)}$, we evaluate h_θ on the supports to obtain an $m \times c$ matrix H with each row being the vector $h_\theta(x_i, u_i)$. Therefore, $H^T W = \langle \mu, h_\theta \rangle$ yields a c -dimensional logit vector. These logits are passed through a softmax and used with the standard cross-entropy loss for classification. A schematic of both models is outlined in Figure 3.

4 Numerical Experiments

In this section, we present a series of numerical experiments designed to evaluate the performance, generalizability, and efficiency of our proposed model across a range of tasks involving 3D data. We consider three distinct scenarios: rotational alignment of 3D human body scans, classification of remeshed surface representations of MNIST digits and classification of facial graph and surface data extracted from the COMA dataset. These experiments demonstrate the flexibility of our model across diverse input types and provide quantitative and qualitative results with comparisons to baseline methods. For each task, we outline the data preprocessing steps, describe the experimental setup, and report results using standard performance metrics. In the final section, we present a series of ablation and robustness experiments to highlight the stability of our model under noise and occlusions. These analyses provide deeper insight into the factors driving the model’s performance and demonstrate its robustness across a range of challenging conditions. All of the models utilize sigmoid activation functions and are trained using the Adam optimizer with a fixed learning rate of 0.005 for 100 epochs to ensure consistency in the presented results. All experiments were conducted on a standard home PC equipped with an Intel 3.2 GHz CPU and a GeForce GTX 2070 GPU (1620 MHz). A Pytorch implementation of the SVarM framework is publicly available on GitHub at <https://github.com/SVarM25/SVarM>.

4.1 Regression for Single Axis Rotation Alignment of Human Bodies

Our first experiment evaluates the effectiveness of our regression model on a toy dataset consisting of 3D human body scans from the FAUST dataset [7] rotated along a fixed axis. In many real-world applications involving 3D data—such as human pose estimation, animation, or medical imaging—scans are often misaligned due to variations in sensor orientation, subject posture, or scanning artifacts. Such rotational misalignment can significantly degrade the performance of downstream tasks. Therefore, estimating and correcting the rotation of 3D scans is a crucial preprocessing step.

To address this, we frame rotational alignment as a regression problem, where the model learns to predict the angle by which a given mesh has been rotated. The goal is to realign each mesh to a canonical upright position. We generate our dataset by applying known rotations to a subset of the FAUST 3D human body scans along a single axis, storing the corresponding angles as labels resulting in 8000 labeled meshes. Our model is trained on 90% of this data and evaluated on the remaining 10%. In Figure 4, we present a selection of dataset samples and demonstrate the model’s ability to accurately predict rotation angles and realign the meshes.

4.2 Regression for Full Rotation Alignment of Human Data

Building on our initial experiment with scalar angle regression, we next evaluate the ability of our model to predict full 3D rotation matrices. While predicting rotation around a fixed axis simplifies the problem, many real-world scenarios involve arbitrary rotations in 3D space. Consequently, modeling the full rotation is essential for general applicability to object alignment.

The training procedure mirrors our previous setup: we generate synthetic data by applying random 3D rotations to FAUST meshes and use the known rotation matrices as supervision. This results in a set of 12840 meshes and train the model on 80% of the data and test it on the remaining 20%. In Figure 5, we display test examples of meshes before and after applying the predicted rotation matrix. In addition, we report quantitative metrics, including the average error and the coefficient of determination for the geodesic distances in $SO(3)$ of the rotation matrices.

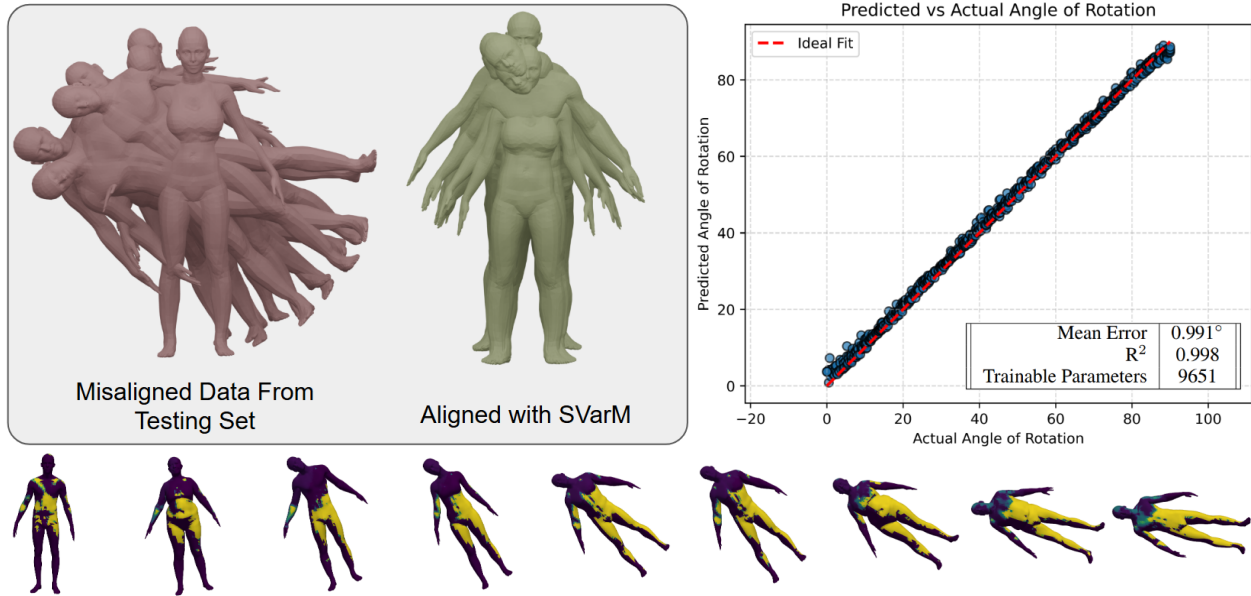


Figure 4: Regression on rotation angle around a fixed axis. We display a selection of human scans from our testing set of misaligned data (red) and present same data rotated by the angle predicted by the SVarM regression model (yellow). Additionally, we plot of the predicted angles against the ground truth on the entire testing set (right) reporting the mean error and correlation coefficient on the entire test set. Lastly, we display the learned function h evaluated on several meshes from the testing data set where the color of each face corresponds to the value of $h(c_f, v_f)$.

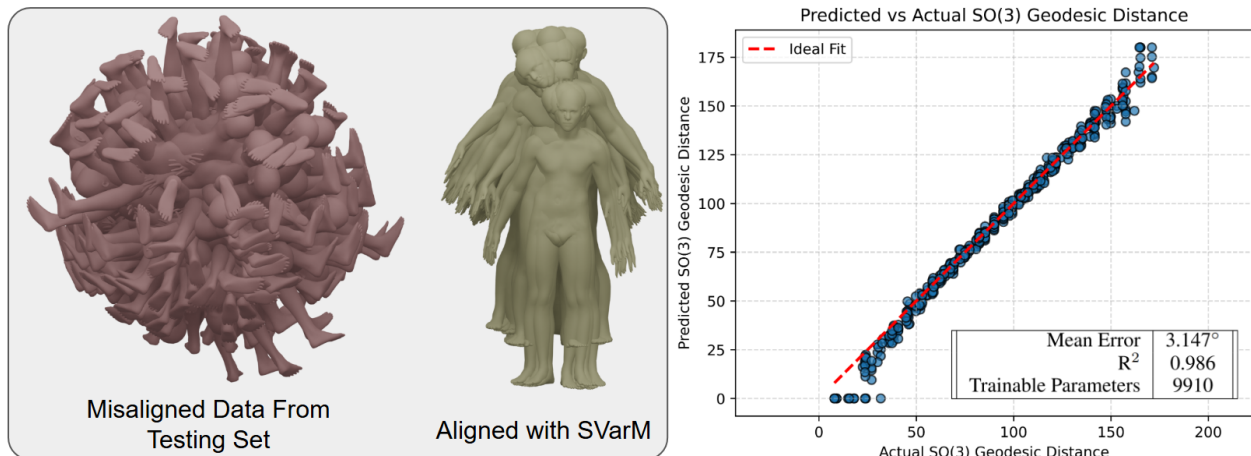


Figure 5: Multidimensional Regression to predict rotation matrices. We display a selection of misaligned data (red) and present same data rotated by the matrix predicted by the SVarM regression model (yellow). Additionally, we plot the geodesic distance in $SO(3)$ from the identity for the predicted matrices against the ground truth matrices (right) reporting the mean error and correlation coefficient on the entire test set.

This experiment demonstrates that our regression framework can be extended from constrained single-axis alignment to general 3D rotational correction, paving the way for integration into more complex pipelines involving arbitrary pose variations and sensor noise.

4.3 Classification of MNIST Digits

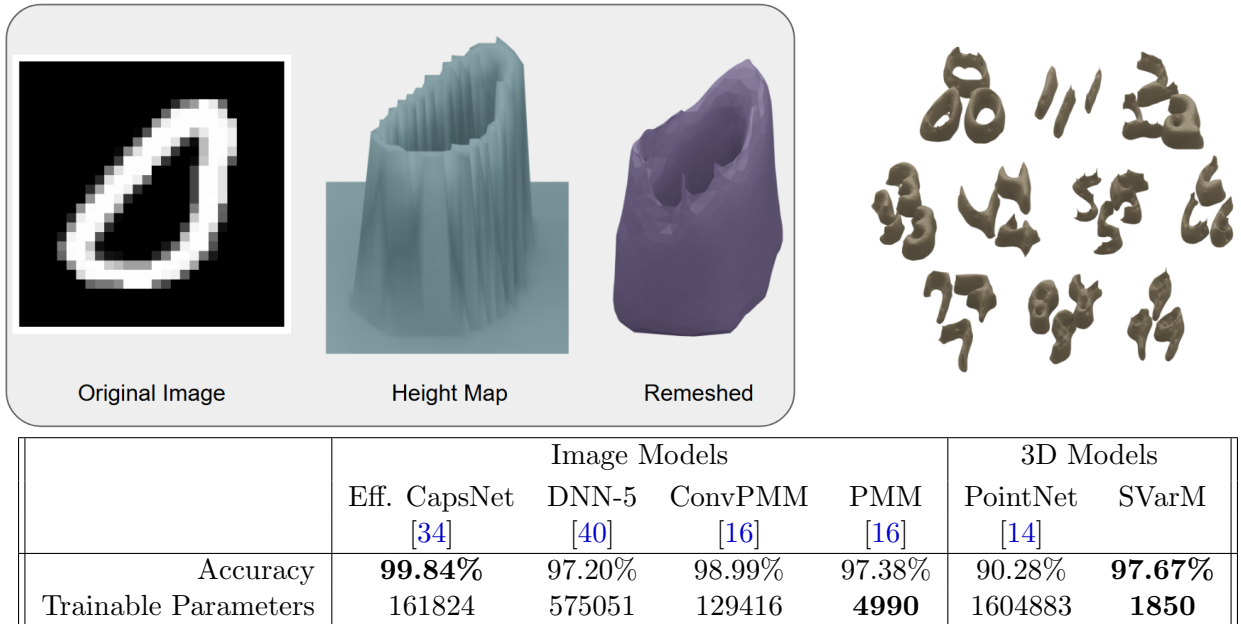


Figure 6: MNIST Surface Construction and Results. An image from the MNIST dataset is converted to a 3D height map surface and remeshed, with examples of this preprocessing shown for each class of the MNIST dataset. We compare several methods operating either on the images or surfaces, reporting accuracy and trainable parameters to highlight our method’s efficiency.

We next evaluate SVarM on the task of classifying handwritten digits from the well-known MNIST dataset. To adapt this image dataset to our framework, following a similar setup to [29], we convert each digit into a 3D surface representation by treating the grayscale pixel values as a height map. We then apply a remeshing operation to generate closed surface meshes corresponding to each digit. A schematic of the conversion process, along with representative examples of the resulting surface meshes, is shown in Figure 6. This pre-processing is not computationally burdensome and requires <20 minutes for the entire MNIST dataset.

We compare our model’s performance to that of several baseline methods that operate directly on the original image data and are designed to be parameter-efficient. While two of these models (Eff. CapsNet and ConvPMM) achieve slightly higher accuracy, they involve significantly more trainable parameters. In contrast, SVarM achieves competitive accuracy while maintaining a much smaller parameter footprint, underscoring its efficiency and suitability for low-resource learning settings.

4.4 Classification of Faces from the COMA Shape Graph Dataset

To further evaluate the effectiveness for classification, we train SVarM on a dataset of shape graphs derived from the CoMA dataset [41], which contains 3D surface scans of human faces. This dataset comprises approximately 21,000 scans of 12 distinct individuals. From each scan, we extract a shape graph by identifying a consistent set of facial landmarks and connecting them via geodesic paths along the surface of the mesh. A schematic illustration of this shape graph construction process is provided in Figure 7. We should note that shape graphs, just as curves, are naturally embedded in the space of varifolds by simple addition in \mathcal{V} of the varifolds associated to each separate branch.

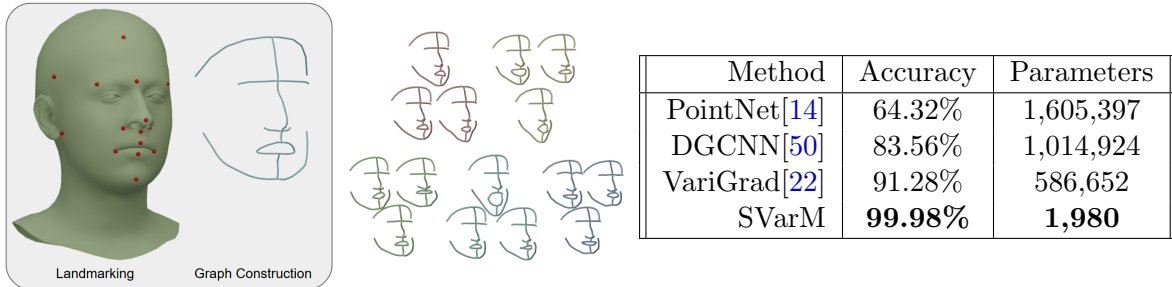


Figure 7: COMA Graph Construction and Results. A schematic illustrating the process of extracting a shape graph from a surface in the COMA dataset with example graphs from 5 of the 12 classes. We compare the classification accuracy and model size for several models evaluated on this dataset.

We split the data into training and test sets, using 80% of the scans for training and the remaining 20% for testing. To assess performance, we compare our proposed model against three baseline models commonly used for 3D shape classification. Our model achieves significantly higher classification accuracy across all metrics. A quantitative summary of these results is presented in Figure 7.

4.5 Robustness Studies

In our final set of experiments, we seek to highlight SVarM’s robustness to imaging noise and missing data. We train our classification model on 80% of the human face surface data from the CoMA dataset. On the testing data, we remove faces from the meshes and report the results on the altered meshes. A visual representation of the meshes with missing faces is shown in Figure 8. We repeat this process, increasing the rate of missing faces and report the classification accuracy in Figure 8.

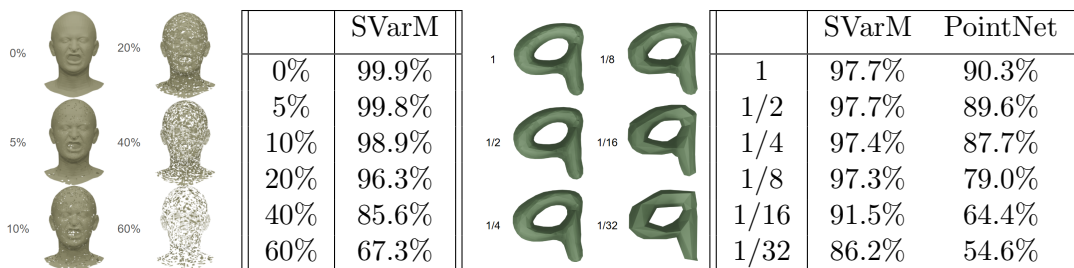


Figure 8: Robustness experiments under different levels of missing data and mesh decimation.

Furthermore, we consider SVarM’s robustness to parameterization by testing the classification model trained on the MNIST digits (c.f. Section 4.3) on down-sampled versions of the testing data. For each mesh in the testing set we apply a mesh decimation operation to reduce the number of faces of the mesh to a fraction of the original and report the results on this down-sampled data. We repeat this process for smaller ratios of total faces and report the classification accuracy in Figure 8. A visual representation of the down-sampled meshes for different ratios of total faces Figure 8.

Finally, we explore the robustness of the SVarM model for a regression problem. We consider the trained regression model discussed in Section 4.1, we apply the face removal process to the testing set and report the results across varying rates of missing faces. As the model’s predictions

are sensitive to the total mass of the input varifolds, its performance deteriorates significantly when a large proportion of faces is removed. To mitigate this issue, we introduce a simple yet effective correction: we normalize the total mass of each varifold to a fixed value. This normalization ensures consistency in the model’s input representations, regardless of the number of removed faces. In Figure 9, we illustrate the impact of missing faces on the regression performance, both with and without normalization, demonstrating the robustness of the SVarM regression model, as well as, the improvement gained by re-normalizing the masses.

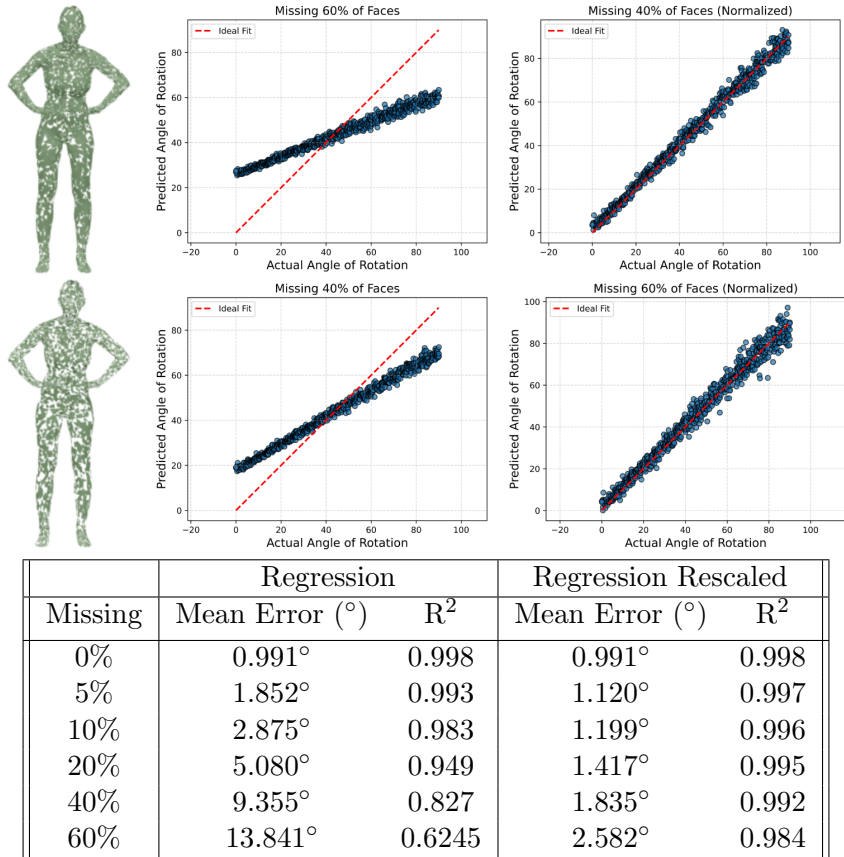


Figure 9: Robustness experiments for regression on single axis angle of rotation under different proportions of missing faces.

5 Conclusion and Limitations

In this work, we propose a learning framework on datasets of curves, surfaces and shape graphs that leverages the (nonlinear) embedding of shapes into varifold space. We focus on this particular measure space as it provides a parameterization-invariant representation of embedded shapes, making the model particularly well-suited for geometric datasets. Analogous to support vector machines—but in the infinite-dimensional setting of varifolds—the SVarM model then learns affine forms $\mu \mapsto \langle \mu, h \rangle + \beta$ to solve regression and classification problems involving 3D geometric data, by approximating a test function $h \in C_0(\mathbb{R}^n \times S^{n-1}, \mathbb{R})$ and bias β . We derive some theoretical guarantees on SVarM’s capacity to approximate arbitrary affine forms, identify conditions under which sets of varifolds or embedded shapes can be linearly separated, and establish stability results

for the model. In addition, we present a series of numerical experiments demonstrating the model’s effectiveness in both regression and classification tasks across various geometric datasets. These experiments highlight the model’s computational efficiency and its robustness to imaging noise, including missing faces and sampling changes. The results also showcase the fact that SVar can achieve comparable (and in some cases superior) accuracy to geometric deep learning models but with an overall much smaller number of trainable parameters, making it in line with recent efforts towards developing lightweight deep learning architectures [31]. Lastly, although the present work was focused on objects such as curves and surfaces, the versatility of the varifold representation makes it possible, in principle, to extend SVarM to other types of geometric data structures, with two cases of interest being high-angular resolution diffusion images [47] and spatial transcriptomics data [45] as these naturally fit the varifold setting.

Limitations: In spite of the above advantages, the SVarM model has certain limitations that we aim to address in future work. In particular, while we demonstrate that any affine function on the space of varifolds can be approximated, the model is not capable of representing non-linear functions on this space. As a result, although we showed how affine functions on \mathcal{V} may be enough to separate disjoint sets of shapes under relatively mild assumptions, there still exist configurations that cannot be classified using this model, c.f. counterexample of Figure 2. In future work, we aim to investigate the learning of non-linear functions on the space of varifolds by combining multiple affine functions with non-linear activation functions, similar to a two-layer multilayer perceptron architecture. This could prove useful in tackling other types of problems than shape classification and regression. Incidentally, we hope to establish a universal approximation theorem for continuous functions on the space of varifolds. Another interesting aspect that has not yet been explored in this paper is the use, during training, of regularization penalties on the weights of the neural network defining h . Such penalties could enforce certain constraints on h so as to potentially increase the qualitative interpretability of the learned test function.

References

- [1] W. Allard. On the first variation of a varifold. *Annals of mathematics*, 95(3), 1972.
- [2] F. Almgren. *Plateau’s Problem: An Invitation to Varifold Geometry*. Student Mathematical Library, 1966.
- [3] A. B. Bal, X. Guo, T. Needham, and A. Srivastava. Statistical analysis of complex shape graphs. *IEEE Transactions on Pattern Analysis and Machine Intelligence*, 2024.
- [4] M. Bauer, M. Bruveris, N. Charon, and J. Møller-Andersen. A relaxed approach for curve matching with elastic metrics. *ESAIM: Control, Optimisation and Calculus of Variations*, 25:72, 2019.
- [5] M. Bauer, M. Bruveris, and P. W. Michor. Overview of the Geometries of Shape Spaces and Diffeomorphism Groups. *Journal of Mathematical Imaging and Vision*, 50(1):60–97, 2014.
- [6] T. Besnier, S. Arguillère, E. Pierson, and M. Daoudi. Toward mesh-invariant 3D generative deep learning with geometric measures. *Computers & Graphics*, 115:309–320, 2023.
- [7] F. Bogo, J. Romero, M. Loper, and M. J. Black. FAUST: Dataset and evaluation for 3D mesh registration. In *Proceedings IEEE Conf. on Computer Vision and Pattern Recognition (CVPR)*, Piscataway, NJ, USA, June 2014. IEEE.

- [8] H. Brézis. *Functional analysis, Sobolev spaces and partial differential equations*, volume 2. Springer, 2011.
- [9] A. M. Bronstein, M. M. Bronstein, and R. Kimmel. Generalized multidimensional scaling: a framework for isometry-invariant partial surface matching. *Proceedings of the National Academy of Sciences*, 103(5):1168–1172, 2006.
- [10] M. M. Bronstein, J. Bruna, Y. LeCun, A. Szlam, and P. Vandergheynst. Geometric deep learning: going beyond euclidean data. *IEEE Signal Processing Magazine*, 34(4):18–42, 2017.
- [11] B. Buet, G. P. Leonardi, and S. Masnou. Weak and approximate curvatures of a measure: a varifold perspective. *Nonlinear Analysis*, 222:112983, 2022.
- [12] W. Cao, Z. Yan, Z. He, and Z. He. A comprehensive survey on geometric deep learning. *IEEE Access*, 8:35929–35949, 2020.
- [13] G. Carlsson. Topology and data. *Bulletin of the American Mathematical Society*, 46(2):255–308, 2009.
- [14] R. Q. Charles, H. Su, M. Kaichun, and L. J. Guibas. Pointnet: Deep learning on point sets for 3d classification and segmentation. In *2017 IEEE Conference on Computer Vision and Pattern Recognition (CVPR)*, page 77–85. IEEE, Jul 2017.
- [15] N. Charon and A. Trouvé. The varifold representation of nonoriented shapes for diffeomorphic registration. *SIAM journal on Imaging Sciences*, 6(4):2547–2580, 2013.
- [16] P. Cook, D. Jammooa, M. Hjorth-Jensen, D. D. Lee, and D. Lee. Parametric matrix models, 2025.
- [17] G. Cybenko. Approximation by superpositions of a sigmoidal function. *Mathematics of control, signals and systems*, 2(4):303–314, 1989.
- [18] H. Edelsbrunner and D. Morozov. Persistent homology. In *Handbook of Discrete and Computational Geometry*, pages 637–661. Chapman and Hall/CRC, 2017.
- [19] J. E. Gerken, J. Aronsson, O. Carlsson, H. Linander, F. Ohlsson, C. Petersson, and D. Persson. Geometric deep learning and equivariant neural networks. *Artificial Intelligence Review*, 56(12):14605–14662, 2023.
- [20] R. Ghrist. Barcodes: the persistent topology of data. *Bulletin of the American Mathematical Society*, 45(1):61–75, 2008.
- [21] U. Grenander. *Elements of pattern theory*. JHU Press, 1996.
- [22] E. Hartman and E. Pierson. Varigrad: A novel feature vector architecture for geometric deep learning on unregistered data. *Eurographics Workshop on 3D Object Retrieval*, 2023.
- [23] E. Hartman, E. Pierson, M. Bauer, M. Daoudi, and N. Charon. Basis restricted elastic shape analysis on the space of unregistered surfaces. *International Journal of Computer Vision*, 133(4):1999–2024, 2025.
- [24] S. Haykin. *Neural networks: a comprehensive foundation*. Prentice Hall PTR, 1994.

- [25] K. Hornik, M. Stinchcombe, and H. White. Multilayer feedforward networks are universal approximators. *Neural networks*, 2(5):359–366, 1989.
- [26] H.-W. Hsieh and N. Charon. Metrics, quantization and registration in varifold spaces. *Foundations of Computational Mathematics*, 21(5):1317–1361, 2021.
- [27] I. H. Jermyn, S. Kurtek, E. Klassen, and A. Srivastava. Elastic Shape Matching of Parameterized Surfaces Using Square Root Normal Fields. In *European Conference on Computer Vision*, page 804–817. Springer, 2012.
- [28] I. Kaltenmark, B. Charlier, and N. Charon. A general framework for curve and surface comparison and registration with oriented varifolds. In *Proceedings of the IEEE conference on computer vision and pattern recognition*, pages 3346–3355, 2017.
- [29] I. Kostrikov, Z. Jiang, D. Panozzo, D. Zorin, and J. Bruna. Surface networks. In *Proceedings of the IEEE conference on computer vision and pattern recognition*, pages 2540–2548, 2018.
- [30] J. Lee, X. Cai, C.-B. Schönlieb, and S. Masnou. Neural varifolds: an aggregate representation for quantifying the geometry of point clouds. *arXiv preprint arXiv:2407.04844*, 2024.
- [31] H.-I. Liu, M. Galindo, H. Xie, L.-K. Wong, H.-H. Shuai, Y.-H. Li, and W.-H. Cheng. Lightweight deep learning for resource-constrained environments: A survey. *ACM Computing Surveys*, 56(10):1–42, 2024.
- [32] Z. Lu, H. Pu, F. Wang, Z. Hu, and L. Wang. The expressive power of neural networks: A view from the width. *Advances in neural information processing systems*, 30, 2017.
- [33] K. V. Mardia and P. E. Jupp. *Directional statistics*. John Wiley & Sons, 2009.
- [34] V. Mazzia, F. Salvetti, and M. Chiaberge. Efficient-capsnet: Capsule network with self-attention routing. *Scientific Reports*, 11:14634, 2021.
- [35] F. Mémoli. Gromov–wasserstein distances and the metric approach to object matching. *Foundations of computational mathematics*, 11:417–487, 2011.
- [36] P. W. Michor and D. Mumford. An Overview of the Riemannian Metrics on Spaces of Curves Using the Hamiltonian Approach. *Applied and Computational Harmonic Analysis*, 23(1):74–113, 2007.
- [37] M. Ovsjanikov, M. Ben-Chen, J. Solomon, A. Butscher, and L. Guibas. Functional maps: a flexible representation of maps between shapes. *ACM Transactions on Graphics (ToG)*, 31(4):1–11, 2012.
- [38] A. Paul, N. Campbell, and T. Shardlow. Sparse Nystrom Approximation of Currents and Varifolds. *arXiv preprint arXiv:2406.09932*, 2024.
- [39] E. Pierson, M. Daoudi, and S. Arguillere. 3d shape sequence of human comparison and classification using current and varifolds. In *European Conference on Computer Vision*, pages 523–539. Springer, 2022.
- [40] E. Pishchik. Trainable activations for image classification. *Preprints*, January 2023.

- [41] A. Ranjan, T. Bolkart, S. Sanyal, and M. J. Black. Generating 3D faces using convolutional mesh autoencoders. In *European Conference on Computer Vision (ECCV)*, pages 725–741, 2018.
- [42] W. Rudin. Functional analysis 2nd ed. *International Series in Pure and Applied Mathematics*. McGraw-Hill, Inc., New York, 1991.
- [43] L. Simon. Introduction to geometric measure theory. *Tsinghua Lectures*, 2(2):3–1, 2014.
- [44] A. Srivastava and E. P. Klassen. *Functional and Shape Data Analysis*, volume 1. Springer, 2016.
- [45] K. M. Stouffer, A. Trouvé, L. Younes, M. Kunst, L. Ng, H. Zeng, M. Anant, J. Fan, Y. Kim, X. Chen, et al. Cross-modality mapping using image varifolds to align tissue-scale atlases to molecular-scale measures with application to 2D brain sections. *Nature communications*, 15(1):3530, 2024.
- [46] Y. Sukurdeep, M. Bauer, and N. Charon. A new variational model for shape graph registration with partial matching constraints. *SIAM Journal on Imaging Sciences*, 15(1):261–292, 2022.
- [47] D. S. Tuch, T. G. Reese, M. R. Wiegell, N. Makris, J. W. Belliveau, and V. J. Wedeen. High angular resolution diffusion imaging reveals intravoxel white matter fiber heterogeneity. *Magnetic Resonance in Medicine: An Official Journal of the International Society for Magnetic Resonance in Medicine*, 48(4):577–582, 2002.
- [48] C. Villani. *Optimal Transport: Old and New*, volume 338. Springer Science & Business Media, 2008.
- [49] A. Virmaux and K. Scaman. Lipschitz regularity of deep neural networks: analysis and efficient estimation. In S. Bengio, H. Wallach, H. Larochelle, K. Grauman, N. Cesa-Bianchi, and R. Garnett, editors, *Advances in Neural Information Processing Systems*, volume 31. Curran Associates, Inc., 2018.
- [50] Y. Wang, Y. Sun, Z. Liu, S. E. Sarma, M. M. Bronstein, and J. M. Solomon. Dynamic graph cnn for learning on point clouds. *Acm Transactions On Graphics (tog)*, 38(5):1–12, 2019.
- [51] L. Younes. *Shapes and Diffeomorphisms*, volume 171. Springer, 2019.

A Ablation Studies

A.1 Choice of measure representation

In this work, we have focused on learning methods that are based on the varifold representation of shapes, i.e. by learning functions on the space $\mathcal{V} = \mathcal{M}(\mathbb{R}^n \times S^{n-1})$, with a shape q being mapped to the varifold $(q, v_q)_* \text{vol } q$. Varifolds combine the information of point position together with the direction of the tangent or normal vector. It is then interesting to compare SVarM against similar approaches but that rely on other possible measure representations. In particular, by marginalizing a varifold with respect to either of the two components S^{n-1} or \mathbb{R}^n , one can quantify the advantage of using both the position and direction information for regression and classification problems. We thus compare the SVarM model to these two alternative measure representation, focusing on surface data. First we consider the space of usual *spatial measures*, $\mathcal{M}(\mathbb{R}^n)$, where $q \mapsto q_* \text{vol } q$. This representation captures only the distribution of points in space (with respect to the local area measure), discarding all directional information. Conversely, we also consider *area measures* in $\mathcal{M}(S^{n-1})$, where $q \mapsto (v_q)_* \text{vol}_q$, which only encodes the distribution of the normal vectors v_q on the sphere independent of the position. Note that these obviously do not allow to uniquely identify a shape but are nevertheless objects central to the field of directional statistics [33].

	1 Axis Rotation Regression		Full Rotation Regression		MNIST Classification
	Mean Error	R ²	Mean Error	R ²	Accuracy
$\mathcal{M}(\mathbb{R}^n)$	3.733°	0.967	4.302°	0.954	90.69%
$\mathcal{M}(S^{n-1})$	6.534°	0.908	7.847°	0.895	79.86%
\mathcal{V}	0.991°	0.998	3.147°	0.986	97.67%

Figure 10: Ablation on Measure Representations of Shapes

Both alternatives encode strictly less geometric information about the shape q compared to the varifold representation. We retrain similar models for each of these measure representations, namely by learning a function on \mathbb{R}^n or S^{n-1} instead of the product space. The results of this comparison are reported in Table 10. They indicate that neither of these simplified models achieves performance comparable to the full SVarM approach.

A.2 Width and depth of the MLP representation of h_θ

We here present a second ablation study related to the architectural choices of the MLP parameterization of the test function h_θ in the SVarM architecture, specifically on the width and depth of the neural network. These results justify the choice of architecture used in the paper.

	MNIST Classification		
	Training Accuracy	Testing Accuracy	Trainable Parameters
mlp(6, 8, 32, 10)	95.51%	95.12%	674
mlp(6, 16, 64, 10)	98.12%	97.67%	1850
mlp(6, 32, 128, 10)	97.28%	97.47%	5738

Figure 11: Ablation on Width of MLP Parameterizations of Test Functions

Increasing the width of the hidden layers generally improves both training and testing accuracy. Notably, the jump from mlp(6, 8, 32, 10) to mlp(6, 16, 64, 10) significantly boosts performance, suggesting that a minimum representational capacity is needed for the model to generalize well.

However, further increasing width to $\text{mlp}(6, 32, 128, 10)$ yields only marginal improvement in test accuracy, despite more than tripling the number of parameters. This indicates diminishing returns and potential over-parameterization. Adding more hidden layers beyond a moderate depth ap-

	MNIST Classification		
	Training Accuracy	Testing Accuracy	Trainable Parameters
$\text{mlp}(6, 64, 10)$	94.75%	95.39%	1098
$\text{mlp}(6, 16, 64, 10)$	98.12%	97.67%	1850
$\text{mlp}(6, 16, 64, 64, 10)$	97.64%	96.18%	6010

Figure 12: Ablation on Depth of MLP Parameterizations of Test Functions

pears to reduce generalization performance. While the two-hidden-layer model $\text{mlp}(6, 16, 64, 10)$ achieves the highest test accuracy, the deeper model $\text{mlp}(6, 16, 64, 64, 10)$ over-fits slightly, achieving higher training accuracy but worse test accuracy. Conversely, the shallow model $\text{mlp}(6, 64, 10)$ under-performs.